JGR Space Physics

RESEARCH ARTICLE
10.1029/2020JA028410

Comparing Electron Precipitation Fluxes Calculated From Pitch Angle Diffusion Coefficients to LEO Satellite Observations

J. A. Reidy[1], R. B. Horne[1], S. A. Glauert[1], M. A. Clilverd[1], N. P. Meredith[1], E. E. Woodfield[1], J. P. Ross[1], H. J. Allison[2], and C. J. Rodger[3]

[1]British Antarctic Survey, Natural Environment Research Council, Cambridge, UK, [2]Helmholtz Centre Potsdam - GFZ German Research Centre for Geosciences, Potsdam, Germany, [3]Department of Physics, University of Otago, Dunedin, New Zealand

Key Points:

- The simulated and measured precipitation are well correlated on the dawnside at $L^* > 5$ for >30 keV electrons
- Additional diffusion is required at higher energies, >100 keV, and on the duskside
- The total precipitating flux typically exceeds that measured by Polar Orbiting Environmental Satellites by a factor between 1 and 10

Correspondence to:
J. A. Reidy,
jadeid70@bas.ac.uk

Citation:
Reidy, J. A., Horne, R. B., Glauert, S. A., Clilverd, M. A., Meredith, N. P., Woodfield, E. E., et al. (2021). Comparing electron precipitation fluxes calculated from pitch angle diffusion coefficients to LEO satellite observations. *Journal of Geophysical Research: Space Physics*, *126*, e2020JA028410. https://doi.org/10.1029/2020JA028410

Received 1 JUL 2020
Accepted 12 FEB 2021

Abstract Particle precipitation is a loss mechanism from the radiation belts whereby particles trapped by the Earth's magnetic field are scattered into the loss cone due to wave-particle interactions. Energetic electron precipitation creates ozone destroying chemicals which can affect the temperatures of the polar regions, therefore it is crucial to accurately quantify this impact on the Earth's atmosphere. We use bounce-averaged pitch angle diffusion coefficients for whistler mode chorus waves, plasmaspheric hiss and atmospheric collisions to calculate magnetic local time (MLT) dependent electron precipitation inside the field of view of the Polar Orbiting Environmental Satellites (POES) T0 detector, between 26–30 March 2013. These diffusion coefficients are used in the BAS Radiation Belt Model (BAS-RBM) and this paper is a first step toward testing the loss in this model via comparison with real world data. We find the best agreement between the calculated and measured T0 precipitation at $L^* > 5$ on the dawnside for the >30 keV electron channel, consistent with precipitation driven by lower band chorus. Additional diffusion is required to explain the flux at higher energies and on the dusk side. The POES T0 detector underestimates electron precipitation as its field of view does not measure the entire loss cone. We demonstrate the potential for utilizing diffusion coefficients to reconstruct precipitating flux over the entire loss cone. Our results show that the total precipitation can exceed that measured by the POES >30 keV electron channel by a factor that typically varies from 1 to 10 for $L^* = 6$, 6.5, and 7.

1. Introduction

The Van Allen radiation belts are highly dynamic regions of trapped particles in the Earth's magnetosphere which can pose a threat to satellites (e.g., Baker et al., 1987). Radiation belt particles also have an impact on our atmosphere when they are lost by precipitation and collide with atmospheric particles, creating ozone-destroying chemical species such as odd nitrogen (NO_x) and odd hydrogen (HO_x) (Thorne, 1977). Both of these species are capable of effecting the atmospheric chemistry in their own right, but ozone concentration plays a significant role in controlling the temperature and dynamics of the atmosphere (Andersson et al., 2014). The full extent of the impact of radiation belt particles on our atmosphere is an outstanding question associated with solar forcing of the climate system (Matthes et al., 2017). Changes in the surface temperatures of the polar regions have been linked with enhanced geomagnetic activity (e.g., Baumgaertner et al., 2011; Seppälä et al., 2009) and it has been shown that particle precipitation can impact regional climate patterns (Rozanov et al., 2005).

There have been several attempts at quantifying the input of electron precipitation into our atmosphere (Andersson et al., 2018; Orsolini et al., 2018), and it is now included as part of the Climate Modeling Intercomparison Project Phase 6 (CMIP6, Matthes et al., 2017). Van de Kamp et al. (2016) and Van de Kamp et al. (2018) obtained data from low-Earth orbiting Polar Orbiting Environmental Satellites (POES) between 2002 and 2012 to create the Ap-Energetic Electron Precipitation (APEEP) model for the CMIP6 data set. The model is focused on the energy range 0.3–1 MeV and runs at a resolution of either 3 h or 1 day. However, this model relies on a POES instrument which does not account for the entire loss cone (e.g., Rodger et al., 2013). Nesse Tyssøy et al. (2016) used wave-particle theory to try and correct for the POES field of view issue and construct a more complete picture of the electron precipitation fluxes across the whole bounce loss cone.

Trapped radiation belt particles can be pitch angle scattered into the loss cone by resonant wave-particle interactions. Particle precipitation is known to increase with geomagnetic activity (e.g., Horne et al., 2009). Meredith et al. (2011) found electron precipitation to increase during the passage of high-speed solar streams; these increases in precipitation were mostly seen on the dawnside, making chorus waves a likely candidate for their scattering. Chorus waves can resonate with electrons of energies from a few hundred eV up to several MeV (Horne et al., 2005) and are predominately observed outside the plasmasphere on the dawnside of the magnetosphere (e.g., Meredith et al., 2003). Lam et al. (2010) found that lower-band chorus plays a dominant role in scattering >30 keV electrons. Plasmaspheric hiss has also been shown to scatter electrons between 20 keV and 2 MeV (Meredith et al., 2004). Plasmaspheric hiss is typically observed in high density regions such as the plasmasphere and plasmaspheric plumes. The wave intensities tend to be strongest during active conditions on the dayside in the region $2 < L^* < 4$. However, during quiet conditions and on the dusk-side, weaker hiss intensities have been observed at higher L^* values (e.g., Meredith et al., 2018). Other sources of precipitation include electromagnetic ion cyclotron (EMIC) waves which generally resonate with electrons >500 keV (Hendry et al., 2017; Summers & Thorne, 2003). Magnetosonic waves have been observed in all MLT sectors outside the plasmasphere but are restricted to the duskside inside the plasmasphere (Meredith et al., 2008); these waves are capable of accelerating trapped electrons to high energies, similar to chorus waves, but they are not thought to contribute to precipitation in their own right as they do not scatter particles directly into the loss cone (Horne et al., 2007). However, magnetosonic waves may contribute to electron loss rates by scattering particles at higher pitch angles which can then be diffused by other plasma waves (e.g., Meredith et al., 2009).

Wave-particle interactions are represented in some radiation belt models (such as those described in Albert et al. [2009], Subbotin et al. [2010], and Glauert et al. [2014]) by diffusion coefficients. In this paper we are using bounce-averaged versions of the pitch angle diffusion coefficients used in the BAS Radiation Belt Model (BAS-RBM) to calculate electron precipitation. The BAS-RBM solves a 3-D Fokker-Planck diffusion equation for the electron flux taking into account radial diffusion, acceleration and losses due to wave-particle interactions, magnetopause shadowing and losses due to atmospheric collisions (Glauert et al., 2014). This model has been extensively used to simulate the trapped radiation belt population, for example, Glauert et al. (2018) recently employed the code to run over a 30 year period and found good agreement with GIOVE-B data. However, the diffusion coefficients used in the BAS-RBM have yet to be utilized to simulate electron precipitation or to calculate the electron flux inside the loss cone. Investigating electron precipitation in a model such as this is important, not only because electron precipitation plays a role in atmospheric chemistry (as discussed above), but also to validate the losses when simulating the trapped population. Very few attempts have been made to quantify loss from radiation belt models. Ferradas et al. (2019) indirectly looked by testing three different loss mechanisms in a radiation belt model but only compared to trapped flux measurements from the Van Allen Probes (VAP). Jordanova et al. (2016) investigated mechanisms for short lived particle injections and their subsequent trapping or loss in a radiation belt model, finding good agreement with observations of both trapped and precipitating flux measured by VAP and POES satellites respectively. In this paper, we will compare precipitating flux calculated using diffusion coefficients with precipitation measurements from POES between 26–30 March 2013. The March 2013 period has been studied by several authors, for example, Xiao et al. (2014), Li et al. (2014), Shprits et al. (2015), Ripoll et al. (2017), Ripoll et al. (2019), and references therein. The analysis presented in this paper is a direct test of the how well the diffusion coefficients used in the BAS-RBM are able to quantify the precipitating flux and therefore a first step toward testing the loss within the BAS-RBM without actually running the BAS-RBM code itself, which is left for a future study.

The pitch angle diffusion coefficients evaluated in this analysis are described in Section 2.1 and the POES electron instruments are outlined in Section 2.2. The theory and method of how we calculate the electron precipitation is given in Section 3. Our results are presented in Section 4, where we give a comparison to the POES data in Section 4.1 followed by a demonstration of how our analysis may one day be implemented to reconstruct the entire loss cone (currently missed by POES) in Section 4.2. The results are discussed and the conclusions presented in Sections 5 and 6 respectively.

2. Data Sets

2.1. Diffusion Coefficients

We have combined bounce-averaged pitch angle diffusion coefficients ($<D_{\alpha\alpha}>$) from whistler mode chorus waves, plasmaspheric hiss and atmospheric Coulomb collisions The contributions from EMIC waves are also included but are negligible at the energies we are looking at and therefore not discussed further in this paper. The hiss and chorus $D_{\alpha\alpha}$ used in the BAS-RBM are calculated from the PADIE code (Glauert & Horne, 2005) which requires the wave power spectrum, wave-normal angle and the ratio of f_{pe}/f_{ce}. The wave power spectra and f_{pe}/f_{ce} are determined by averaging observations from multiple spacecraft which have been binned by frequency, L^*, MLT, magnetic latitude and geomagnetic activity level. Therefore, the diffusion coefficients used in this study are averaged diffusion coefficients and not event-specific as in, for example, Ripoll et al. (2019).

For the chorus waves, we are using pitch angle diffusion coefficients derived from a new wave database using data from seven satellites presented in Meredith et al. (2020). The calculations for $<D_{\alpha\alpha}>$ are done in nearly the same way as Horne et al. (2013) with a few differences: a data driven version of PADIE that takes a frequency spectrum rather than Gaussian parameters has been used, there is no interpolation in L^* and the f_{pe}/f_{ce} has a 1 h MLT grid rather than 3 h. As in Horne et al. (2013), the statistical wave power maps used in calculating the average chorus wave diffusion coefficients exclude wave observations that are thought to be inside the plasmapause; this is inferred from a combination of observations of plasmapause crossings (where available) and a plasma density model (Carpenter & Anderson, 1992). A mask is also applied to the wave power map whereby anything inside a modeled plasmapause is set to zero (Meredith et al., 2018). The wave-normal angle spectrum was assumed to be a Gaussian in the tangent of the wave-normal angle (as in Glauert & Horne, 2005; Horne et al., 2013).

The diffusion coefficients for the hiss waves were derived as described in Glauert et al. (2014) using an updated wave model based on data from eight satellites described in Meredith et al. (2018). These $<D_{\alpha\alpha}>$ were calculated using a variable wave-normal angle, where the peak wave-normal angle is field aligned at the equator and then increases with increasing latitude (Glauert et al., 2014). Similar to the chorus wave data, the wave power outside the plasmapause is excluded by a mask (Meredith et al., 2018).

The top three rows of Figure 1 show global maps of the chorus and hiss $<D_{\alpha\alpha}>$ for low, moderate, and high geomagnetic activity levels, as specified by Kp, for the electron energies at 30, 100, and 300 keV. The values of $<D_{\alpha\alpha}>$ used in this study, and shown in Figure 1, have been averaged over the loss cone at each L-shell (the loss cone angle has been calculated assuming a dipole magnetic field and an atmospheric altitude of 100 km, as is done in the PADIE calculations). The yellow line in the figures marks the modeled location of the plasmapause (Lpp); this line is shown dashed between 14 and 22 MLT as more work is needed to determine the average location of the plasmapause in this region. As mentioned above, this modeled Lpp was used as a mask to separate the wave power inside and outside the plasmapause when calculating the diffusion coefficients and therefore the yellow line in the figures separates the hiss and chorus $<D_{\alpha\alpha}>$. For reference, the bottom row of Figure 1 shows the values of the f_{pe}/f_{ce} used in the calculations of the hiss and chorus $<D_{\alpha\alpha}>$, again separated by the Lpp.

Figure 1 demonstrates that the chorus $<D_{\alpha\alpha}>$ have a strong MLT dependence which peaks on the dawnside, consistent with enhanced chorus power and low values of f_{pe}/f_{ce} in this region during active conditions (e.g., Meredith et al., 2003). The $<D_{\alpha\alpha}>$ outside the plasmapause are strongest for 30 keV electrons, suggesting that chorus waves are better at scattering electrons at lower energies. During active conditions the region of strongest diffusion for 30 keV electrons moves to higher L shells in the pre-noon sector. This is consistent with the behavior of the peak in the chorus wave power which also shows a similar dependence on MLT in the equatorial region (Meredith et al., 2020).

As discussed above, the $<D_{\alpha\alpha}>$ for chorus and hiss waves have pitch angle, energy, L-shell, MLT and geomagnetic activity dependence. The top two panels of Figure 2 show the chorus and hiss diffusion coefficients $<D_{\alpha\alpha}>$ as a function of pitch angle for 30 keV electrons at $L^* = 5.5$ during high geomagnetic activity levels ($4 < Kp < 7$) for different MLT sectors (shown in different colors). The loss cone angle is shown by a vertical dashed line. Over this limited pitch angle range close to the loss cone, the diffusion coefficients

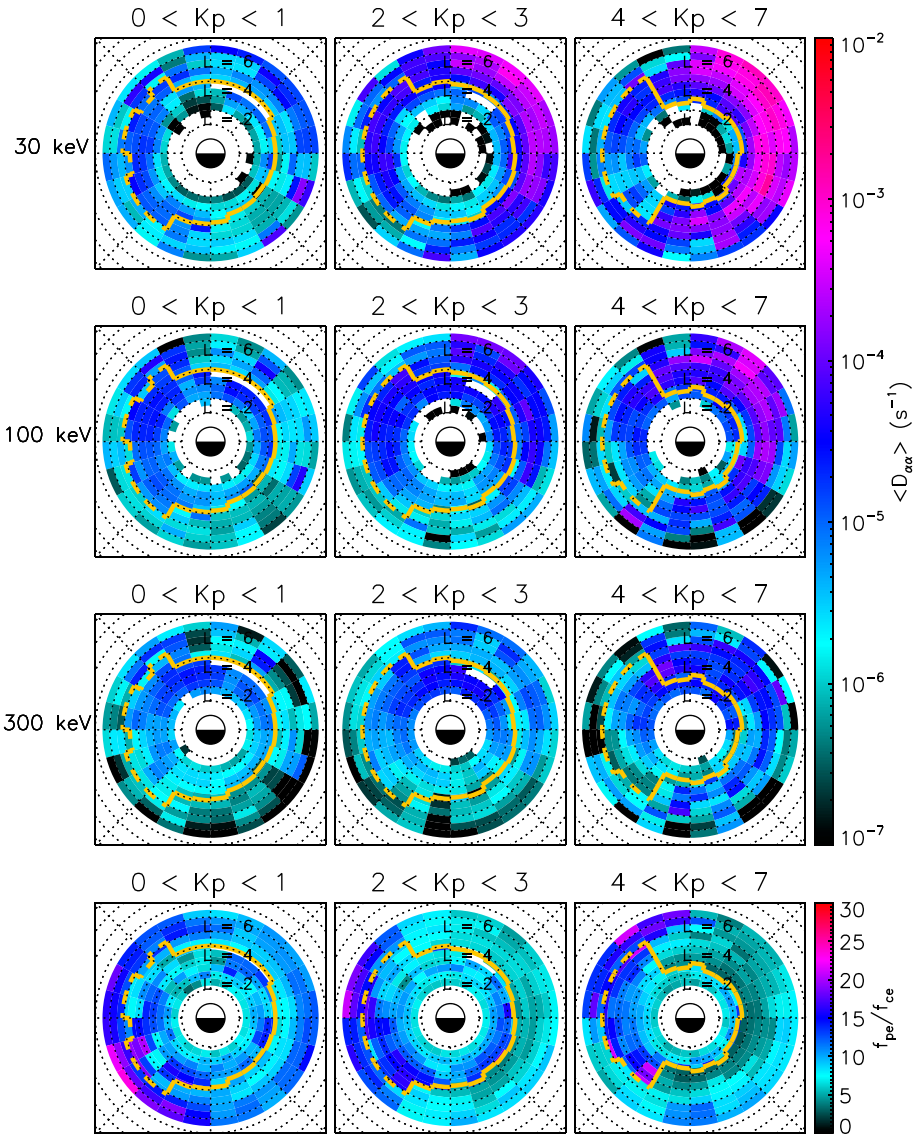

Figure 1. Top three rows showing the global distribution of the bounce-averaged diffusion coefficients for chorus waves and hiss waves at electron energies of 30, 100, and 300 keV for low, moderate and high geomagnetic activity levels averaged over the dipolar loss cone. The yellow line shows the Lpp which marks the boundary between the hiss and chorus <$D_{\alpha\alpha}$>. The bottom row shows the f_{pe}/f_{ce} used to calculate the . Noon is at the top and dawn is to the right.

for both chorus and hiss are fairly flat. Both waves show strong MLT dependence with the hiss <$D_{\alpha\alpha}$> only contributing on the duskside (and inside the plasmasphere) and the <$D_{\alpha\alpha}$>'s for chorus are strongest on the dawnside (as can be seen in Figure 1). The strong diffusion limit at $L^* = 6$ and $E = 30$ keV is 3.7×10^{-3} s^{-1} (calculated following Summers and Thorne [2003] and indicated by a dotted line in Figure 2), showing that the diffusion driven by chorus approaches the strong diffusion limit on the dawnside at this energy, L-shell and geomagnetic activity level.

The bottom panel of Figure 2 shows the $D_{\alpha\alpha}$ for the coulomb collisions, these $D_{\alpha\alpha}$ are calculated as a function of energy and L-shell, as outlined in Abel and Thorne (1998). The neutral and plasma densities are taken from the NRLMSISE-00 (Picone et al., 2002) model and the GCPM (Gallagher et al., 2000) respectively. In these calculations, the edge of the loss cone is defined to be where the energy of the electrons has dropped by $1/e$ of its original value due to collisions with atmospheric particles. The loss timescales (τ_C) is set to be a quarter of the bounce time in the loss cone and infinite elsewhere. Figure 2 demonstrates that the collision $D_{\alpha\alpha}$ only contribute inside or near to the 100 km loss cone and fall off rapidly outside. We neglect energy

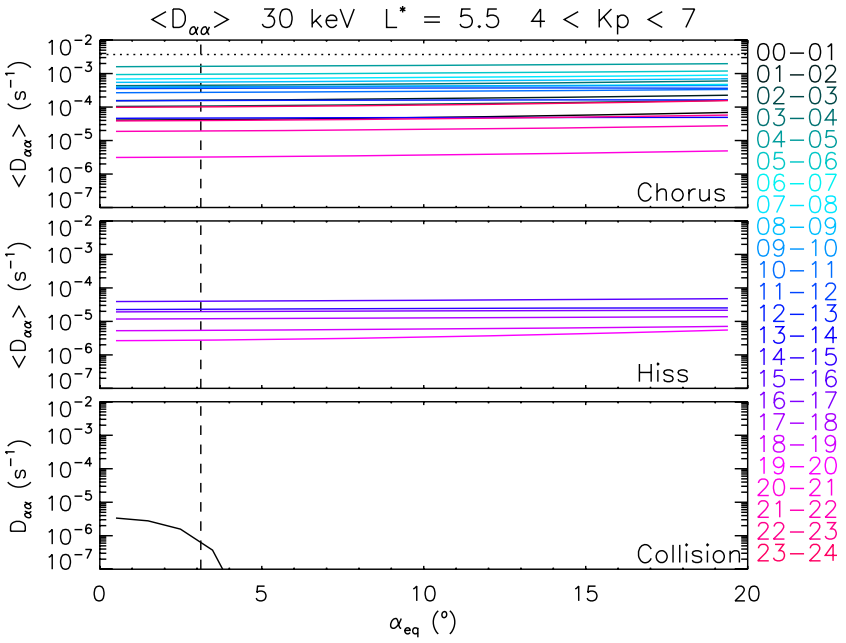

Figure 2. Bounce-average pitch angle diffusion coefficients ($<D_{\alpha\alpha}>$) from the BAS-RBM at L^* = 5.5 and 4 < Kp < 7, shown for chorus and hiss waves (top two panels) and coulomb collisions (bottom panel). The $<D_{\alpha\alpha}>$ for chorus and hiss are shown for MLT sectors, indicated on the right hand side on the plot. The angle of the loss cone is shown by a vertical dashed line and the strong diffusive limit is shown by a dotted line in the top panel.

diffusion of coulomb collisions in this study but note it could be important at larger pitch angles as shown by Selesnick (2012) and Cunningham et al. (2018).

2.2. The Polar Orbiting Environmental Satellites (POES)

The POES constellation of spacecraft are in Sun-synchronous orbits at a low altitude of 800–850 km altitude. We have obtained data from the Space Environment Monitor (SEM-2) package on board POES spacecraft NOAA15 to 19. The SEM-2 package includes the Medium Energy Proton and Electron Detectors (MEPED), which has two electron solid state detectors capable of measuring electrons between 30 and 2,500 keV in three integral channels (>30, >100, and >300 keV) (Evans & Greer, 2004). Each channel is known to suffer from proton contamination (e.g., Yando et al., 2011), we are evaluating data which have been corrected for this using the bow tie method described in Lam et al. (2010). Both detectors are ±15° wide, one centered 9° from local zenith (the 0° detector, T0) and the other mounted perpendicular to this (the 90° detector, T90 anti-parallel to the spacecraft velocity). The 0° detector predominately measures electrons in the bounce loss cone for $L > 1.4$ (Rodger et al., 2010b). The 90° detector measures a mixture of electrons in drift and bounce loss cones and those that are trapped (Rodger et al., 2010a).

To make sure we are only evaluating data from T0 when its measuring precipitating flux and T90 when its measuring flux outside the loss cone in our analysis, we make sure the equatorial loss cone angle (α_0) is greater than the field of view of the T0 detector and less than the field of view of the T90 detector. We calculate α_0 at each time using

$$\alpha_0 = sin^{-1}\left(\sqrt{\frac{B_{eq}}{B_{POES\_FOFL}}}\right), \quad (1)$$

where B_{eq} is the magnetic field strength at the equator (given by Olson-Pfitzer quiet time model [Olson & Pfitzer, 1977]) and $B_{\mathrm{POES\_FOFL}}$ is the field strength at the foot of the field line at the location of POES (assumed to be 100 km, from the IGRF). The T0 and T90 fields of view are projected to the equator using

$$\alpha_{eq} = sin^{-1}\left(\sqrt{\frac{B_{eq}}{B_{POES}}}\sin(\theta_{T90/0} \pm 15°)\right), \quad (2)$$

where $\theta_{T90/0}$ are the central pitch angles of each detector (of which we take ±15° to take into account for the entire field of view) and B_{POES} is the magnetic field strength at the height POES (from the IGRF). We note that this does not guarantee T90 is measuring trapped flux as it could be measuring flux in the drift loss cone.

3. Calculation of POES Precipitating Flux

To calculate the precipitating flux measured by POES, we are using a steady state solution to a Fokker-Planck equation for pitch angle diffusion from Kennel and Petschek (1966), given by:

$$J_{eq}(E,\alpha_{eq}) = N\, S(E)\, D_{\alpha\alpha}(\alpha_0)^{-1}\left[h(\alpha_0) + \ln\left(\frac{\sin\alpha_{eq}}{\sin\alpha_0}\right)\right], \quad (3)$$

outside the loss cone ($\alpha_0 \le \alpha_{eq} \le \frac{\pi}{2}$), and

$$J_{eq}(E,\alpha_{eq}) = N\, S(E)\, D_{\alpha\alpha}(\alpha_0)^{-1}\, h(\alpha_{eq}), \quad (4)$$

inside the loss cone ($\alpha_{eq} \le \alpha_0$), where

$$h(\alpha_{eq}) \equiv \frac{\sqrt{D_{\alpha\alpha}(\alpha_0)\tau}}{\alpha_0}\left[\frac{I_0\left(\frac{\alpha_{eq}}{\sqrt{D_{\alpha\alpha}(\alpha_0)\tau}}\right)}{I_1\left(\frac{\alpha_0}{\sqrt{D_{\alpha\alpha}(\alpha_0)\tau}}\right)}\right]. \quad (5)$$

$J_{eq}(E, \alpha_{eq})$ is the equatorial flux distribution for electrons, E is the energy, α_{eq} are the equatorial pitch angles, τ the bounce loss time (assumed to be a quarter of a bounce period), N is a normalization factor, $S(E)$ is the source of particles (N and $S(E)$ will be defined in Section 3.1), I_0 and I_1 are modified Bessel functions and $D_{\alpha\alpha}(\alpha_0)$ are the combined bounce-averaged pitch angle diffusion coefficients from the BAS-RBM (described in Section 2.1) evaluated at the loss cone. The value of $D_{\alpha\alpha}(\alpha_0)$ is determined at each time depending on the L^*/MLT location of the spacecraft and the current geomagnetic activity level.

Despite being a solution for a steady state, this application has been validated in several studies by comparison to different data sets (for example, the POES electron observations in Li et al. [2013] and Nesse Tyssøy et al. [2016]). Furthermore, this steady state solution is independent of the scattering mechanism for pitch angle diffusion (Theodoridis & Paolini, 1967) and therefore we can use the combined diffusion coefficients from the BAS-RBM (described in Section 1.2).

Figure 3 demonstrates the differential flux (J_{eq}) calculated from Equations 3 and 4 for a range of diffusion coefficients (indicated in the bottom right corner of Figure 3d) at $L^* = 4, 5, 6, 7$ and for 30 keV (solid lines) and 100 keV (dashed lines) electrons. Here we have adopted a common source term of $S(E) = 10^5$ cm^{-2} sr^{-1} s^{-1} keV^{-1} at $\alpha_{eq} = \frac{\pi}{2}$ as an example of a reasonable source term and assumed at dipolar loss cone (shown by the vertical dotted black line). The strong diffusion limit has been calculated following Summers and Thorne (2003) for 30 keV (red) and 100 keV (yellow) at each L^* and is shown at the top of each figure; these figures show at the strong diffusion limit, we have a near isotropic distribution between the trapped and the precipitating flux. As the diffusion coefficients decrease, the flux in the loss cone drops off exponentially. The median field of view (FOV) of the POES T90 and T0 (which have been projected to the equator using Equation 2) during the event investigated in this paper (26–30 March 2013) are indicated by gray shaded regions for each L^*. This demonstrates that the FOV of the T0 detector is not measuring the entire loss cone

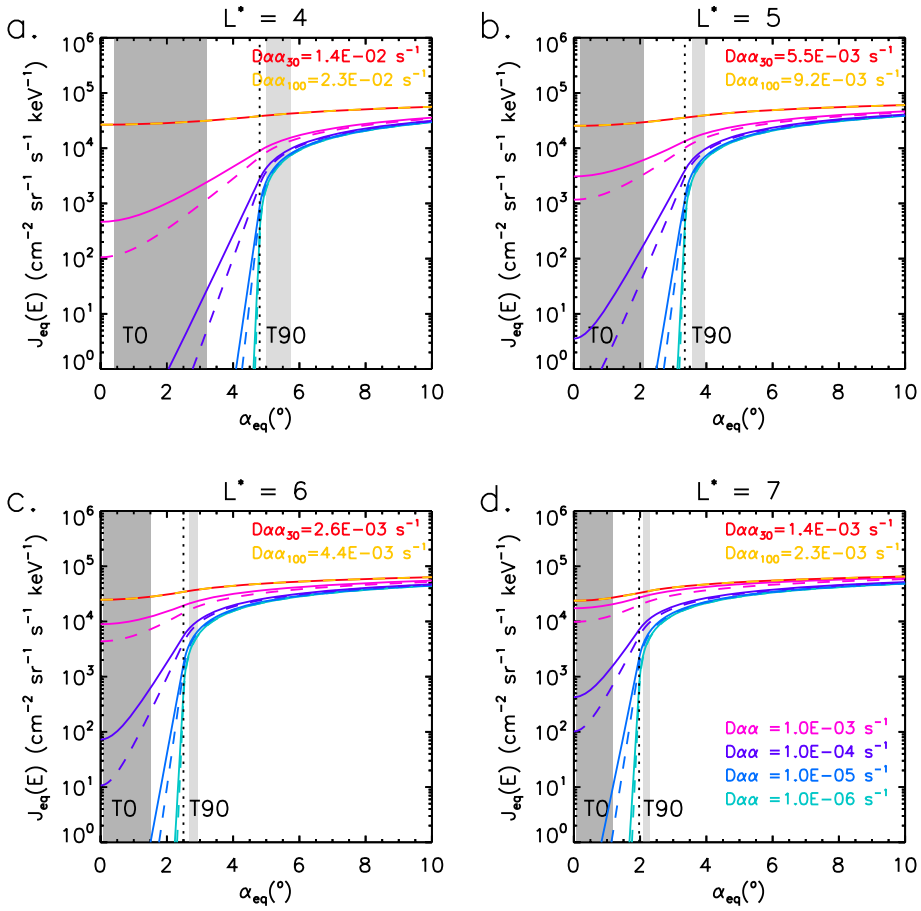

Figure 3. Each panel shows the differential flux calculated from Equations 3 and 4 at for 30 keV (solid) and 100 keV (dashed) electrons for a range of diffusion coefficients (given in the bottom right figure) at (a) $L^* = 4$, (b) $L^* = 5$, (c) $L^* = 6$, and (d) $L^* = 7$. The red and yellow lines show the flux calculated during the strong diffusion limit (values for which are given at the top of each figure). Median values for the T90 and T0 field of view each L^* are indicated by gray shaded regions.

and therefore any precipitating flux measurements from this channel will be an underestimate unless the loss cone is full, as previously shown by Rodger et al. (2013). Furthermore, the T90 FOV is very close to the loss cone and therefore when selecting our data points for analysis we always make sure the T90 FOV is outside the bounce loss cone as discussed above. We also note that the trapped flux drops significantly just outside the loss cone, this is taken into account as discussed below.

3.1. Energy Spectrum and Source Term

To get the source term and normalization factor, $N\,S(E)$, in Equations 3 and 4, we convert the T90 measurement of the trapped integral flux to differential flux by assuming a kappa-type function (Whittaker et al., 2013; Xiao et al., 2008) for the energy spectrum of the source flux ($J_S(E)$). By adopting similar notation to Equation 10 in Glauert et al. (2018) this gives

$$J_S(E) = m_0 \frac{E(E+2E_0)}{E_0} P_1 \left(1 + \left(\frac{E}{P_2}\right)^2\right)^{-(\kappa+1)} \mathrm{d}E, \tag{6}$$

where E_0 is the particle rest energy, given by m_0c^2 (m_0 is the rest mass and c is the speed of light). We adopt $\kappa = 5$, as in Li et al. (2013), and solve for P_1 and P_2. For P_2, we use an iterative method, whereby we take the difference of the ratio between the POES T90 > 30 keV and >100 keV detector measurements and the

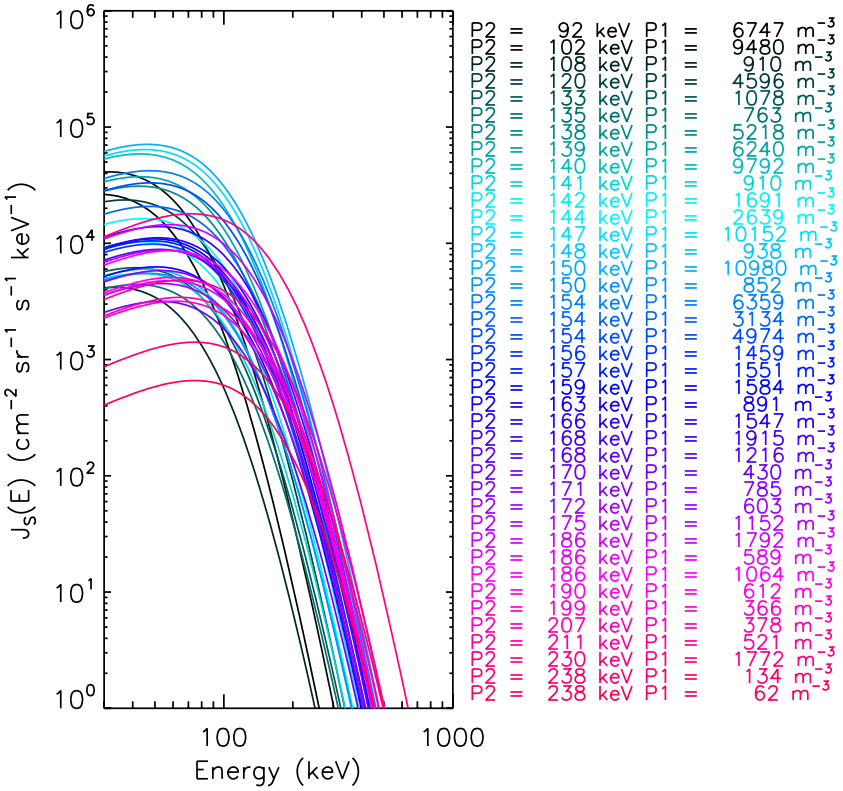

Figure 4. Differential electron flux spectra fitted to a kappa-type distribution using Equation 6. The values of P_1 and P_2 are shown for each spectra at each time step (indicated by the color). This spectra is evaluated at θ_{T90}, which corresponds to the pitch angle location of the T90 detector.

ratio of Equation 6 integrated between 30 keV to 2.5 MeV and 100 keV to 2.5 MeV (to simulate the POES detectors) until the difference is less than 1×10^{-3}. We then take this value of P_2 and the >30 keV T90 measurement to solve for P_1 and obtain an overall kappa-type fit for the differential flux. Figure 4 demonstrates the differential flux estimated from this method for one of the L^*/MLT sectors in our analysis ($L^* = 6$, 09–12 MLT), where the P_1 and P_2 solutions are indicated for each spectra at each time step.

We use this distribution to solve for $N\,S(E)$ by rearranging Equation 3 as follows:

$$N\,S(E) = \frac{J_S(E)}{D_{\alpha\alpha}(\alpha_0)^{-1}\left[h(\alpha_0) + \ln\dfrac{\sin(\alpha_{eq})}{\sin(\alpha_0)}\right]}. \tag{7}$$

Here we take the central pitch angle of the T90 detector (θ_{T90}) as α_{eq}, which has been transformed to the equator using Equation 2.

Note that the calculation of $N\,S(E)$ is for the equatorial pitch angle corresponding to that observed by the POES T90 detector and not that at $\alpha_{eq} = \dfrac{\pi}{2}$. This therefore takes into account the change in flux for different diffusion rates just outside the loss cone in the steady state solution.

By employing this method to obtain the source term, we are not using the flux output calculated by the BAS model but instead our best assessment of what the actual flux was from the POES T90 experimental measurements. Therefore, the analysis presented in this paper is a test of the BAS wave diffusion matrix and not the model itself.

3.2. Comparing to POES T0 Measurement

We calculate the theoretical flux measured by the POES T0 detector by integrating the differential flux ($J_{eq}(E, \alpha_{eq})$ from Equations 3 and 4) inside the FOV of the POES detectors based on an equation from Walt (1994) given by

$$J_{calc}(E > E_{th}) = \frac{\int_{E_{th}}^{E_{max}} \int_0^{2\pi} \int_0^{\beta} J_{eq}(E, \alpha_{eq}) A \sin\eta \, \mathrm{d}\eta \mathrm{d}\psi \, \mathrm{d}E}{\int_0^{2\pi} \int_0^{\beta} A \sin\eta \, \mathrm{d}\eta \, \mathrm{d}\psi}, \tag{8}$$

where A is the detector area (stated to be 25 mm^2 for the solid-state detector in the POES electron detector telescope in Evans and Greer [2004]) and E_{th} and $E_{\max}$ are the thresholds of the POES electron detectors (30, 100, and 300 keV) and maximum energy (taken to be 2.5 MeV as a representative nominal value) respectively. A similar approach was adopted for comparison with POES data in Li et al. (2013). The value of J_{calc} will be directly compared with POES measurements later in this paper.

The pitch angle of the detector is given by

$$\cos\alpha = \cos\theta\cos\eta + \sin\theta\sin\eta\cos\psi, \tag{9}$$

where α is the local pitch angle at the POES detectors, θ is the central pitch angle of the POES detector (provided with the data), β is the half-angle of detector acceptance (15° for the POES T0 detector) and η and ψ are integrated over the field of view of the POES detector (as demonstrated by Figure 1b of Li et al. [2013]). We transform α to the equator (by Equation 2) before using in Equations 3 and 4 to calculate the equatorial flux.

In Equation 8, we are effectively dividing a count rate by a geometric factor (GF). The POES documentation states that the count rate should be divided by GF = 0.01 to get the integral flux (Evans & Greer, 2004) (updated modeling of the MEPED instrumentation and the electron telescope geometric factors shows this is reasonable for most energies (Yando et al., 2011)). However, the GF was calculated for an isotropic electron flux (Evans & Greer, 2004) whereas the flux in the loss cone can be highly anisotropic (as demonstrated in Figure 3). Furthermore, the GF takes into account the sensitivity of the detector which we do not need to do as we are calculating true theoretical count rates from Equation 8 and not count rates as measured by an instrument. In the anisotropic case here we compute the flux that would be measured numerically and use an effective geometric factor (GF*), where $GF^* = \int_0^{2\pi}\int_0^{\beta} A \sin\eta \mathrm{d}\eta \mathrm{d}\psi = 2\pi \cdot \mathrm{A} \cdot (1 - \cos\beta)$.

4. Results

4.1. POES Comparison

We present precipitation flux observations from NOAA15, 16, 17, 18, and 19 between 26–30 March 2013, shown in Figure 5. The data from each spacecraft have been combined by taking the mean of the measurements over 0.5 L^*, for example at a quoted $L^* = 6$ we have averaged the flux data between 6 and 6.5 L^* from each spacecraft in both hemispheres; this is done to match the L^* bins of the $<D_{\alpha\alpha}>$ used in the analysis. The L^* associated with the POES data in this paper were calculated using the International Geomagnetic Reference Field and the T96 external field (Tsyganenko, 1995), as in Allison et al. (2018). This event captures minor geomagnetic storms, with low/moderate Dst level and moderate/high Kp level (high for 12 h on March 27) as shown in the bottom panel of Figure 5, and avoids a solar proton event seen earlier in the month. To minimize the chance of proton contamination, we have omitted times where the POES satellites were within the longitude of the South Atlantic anomaly as in that area protons overwhelm the electron observation from both telescopes (e.g., Figure 4 of Rodger et al. [2013]). The top three panels of Figure 5 give an overview of the POES T0 measurements at $L^* = 4, 5, 6$ for the three electron channels; it can be seen that the precipitating fluxes are greatest at $L^* = 6$ for the >30 keV channel during periods when the geomagnetic activity is highest.

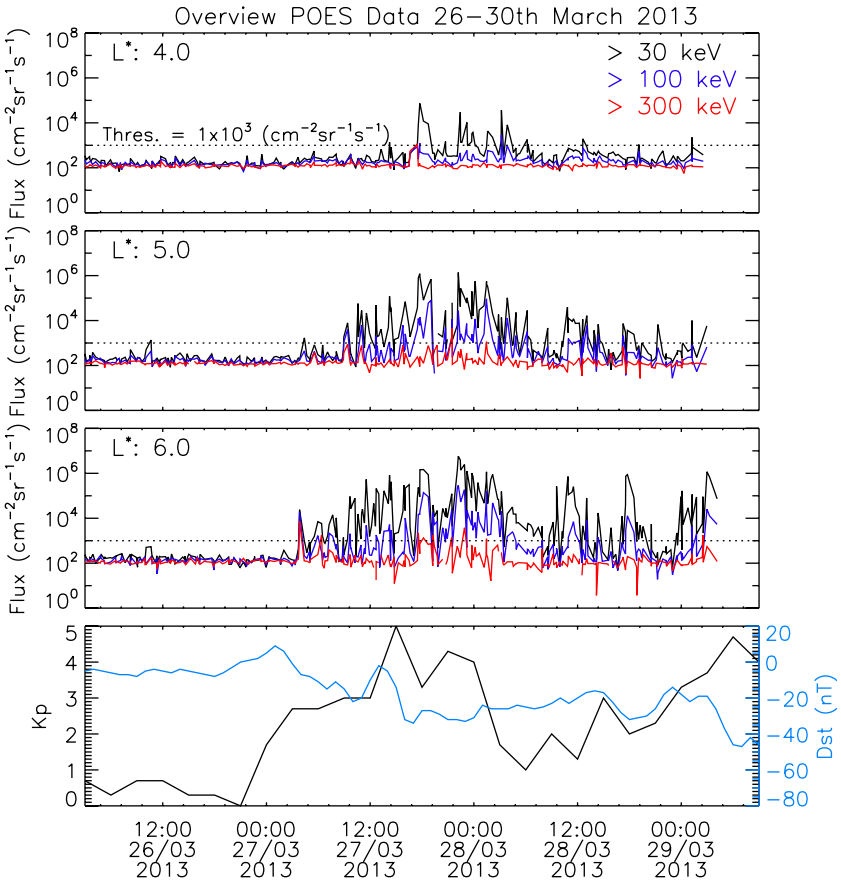

Figure 5. The top three panels show the POES flux for the >30 keV (black), >100 keV (blue), and >300 keV (red) electron channels at $L^* = 4$, 5, and 6 respectively. The dotted horizontal line shows the noise threshold. The bottom panel gives the geomagnetic Kp (black) and Dst (blue) indices during this event.

For our analysis, we adopt a strict noise threshold of 1,000 $cm^{-2}\ sr^{-1}\ s^{-1}$ for each electron channel, indicated by a horizontal dotted line in the top three panels. It can be seen that during this event, the precipitating flux measured by the >300 keV channel (red) is predominately below this line and will therefore not be considered for the remainder of this paper.

Figures 6a and 6b show the agreement between our calculated T0 precipitation (J_{calc}, from Equations 3 to 8) and the POES T0 (blue line) and T90 measurements (red line) at $L^* = 7$ between 09–12 MLT and $L^* = 5$ between 21–24 MLT respectively. The calculated T0 flux, shown by black crosses, remains below the flux measured by T90 as required. The bottom panel in each figure shows the Kp and the selected diffusion coefficients for 30 keV (crosses) and 100 keV (triangles) used at each time for our calculation; these are representative values for each energy channel, >30 keV (top panel) and >100 keV (middle panel), as the flux is highest for these energies and therefore these diffusion coefficients dominate our flux calculation. The $<D_{\alpha\alpha}>$ are selected at each energy depending on the location of POES in terms of L^* and MLT at each time step (the $<D_{\alpha\alpha}>$ have 0.5 L^* and 1 h MLT resolution, however we do our analysis over 3 h of MLT to increase the number of data points in each L^*/MLT sector). The activity level of the $<D_{\alpha\alpha}>$ is chosen depending on either the current Kp or the Kp averaged over the last 12 h, whichever is highest, to take into account the time history of the system (referred to as Kp* in later plots). We have also averaged the $<D_{\alpha\alpha}>$ over all pitch angles within the loss cone (see Figure 2).

The top panel of Figure 6a shows good agreement between the measured and calculated T0 precipitation for the >30 keV integral flux channel. We note, at this L-shell and MLT location that these results are consistent with chorus wave driven diffusion, this is will be discussed more below. For the >100 keV channel (middle panel), our calculations are underestimating the precipitation. Figure 6b, on the other hand, shows

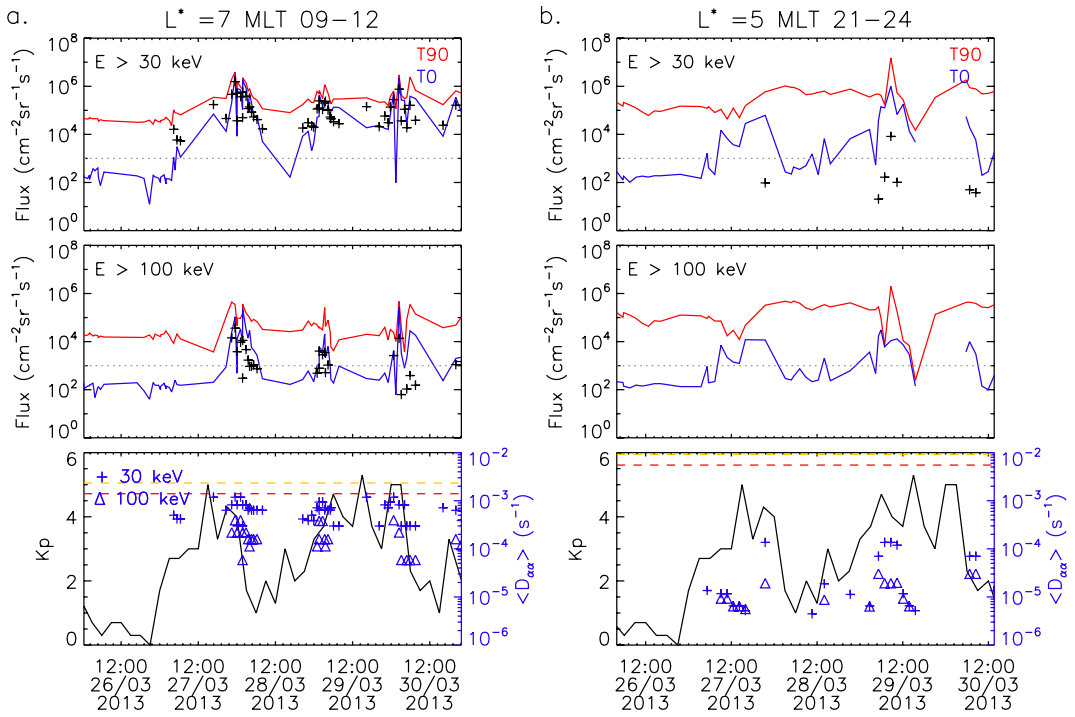

Figure 6. Figure showing the flux measured by the POES electron detector for the >30 keV (top) and >100 keV (middle) channels for the 0° (blue) and 90° (red) telescopes and the Kp index during the event (bottom) for (a) $L^* = 7$, 09–12 MLT and (b) $L^* = 5$, 21–24 MLT. The black crosses in the top two panels show the calculated precipitation from the BAS-RBM. The blue crosses and triangles in the third panel show the diffusion coefficients selected at each time for 30 and 100 keV respectively. The red and yellow dashed lines represent the strong diffusion limit for the 30 and 100 keV electrons respectively. In (b) for >100 keV, the simulated T0 flux falls below the *y*-axis (cf., Figure 9).

us an example where our calculated flux is much lower than that measured by POES T0, with much of the calculated T0 precipitation below the y-range on the plot axis (all for the >100 keV channel). We can see from the bottom panel Figure 6b that, at this MLT and L-shell, the BAS wave model predicts a large number of the $<D_{\alpha\alpha}>$'s to be between 10^{-5} and 10^{-6} s^{-1} (particularly for 100 keV). Figure 3b (blue and cyan lines) shows these values for the $D_{\alpha\alpha}$ correspond to an exponential drop off in the flux in the loss cone which is outside the median FOV of the T0 detector during this event; this will therefore result in our method (Equations 3–8) predicting low precipitating fluxes at these times. Conversely, the bottom panel of Figure 6a shows, at times, the BAS diffusion coefficients are approaching the strong diffusive limit from (Summers & Thorne, 2003) (shown by red and yellow lines dashed lines for the 30 and 100 keV electrons respectively) for $L^* = 7$, between 09–12 MLT. At these times, the T0 measurements are reaching the T90 measurements, suggesting the trapped and precipitating fluxes are comparable, as expected during strong diffusion and demonstrated in Figure 3d by the yellow and red lines. These results suggests we are getting better agreement between the calculated and measured T0 precipitation during periods of strong diffusion, that is, when there is more flux in the loss cone.

Figures 7a and 7b show scatter plots of the calculated and measured T0 precipitation for the two L^*/MLT sectors presented in Figure 6. Figure 7a demonstrates our method simulates the T0 measurements well in this L^*/MLT sector, with most of the points lying on or close to the $x = y$ line for the >30 keV channel. For the >100 keV channel we predominately underestimate the precipitating flux. Figure 7b shows we are consistently underestimating the precipitation in the 21–24 MLT sector for both energy channels, with a large spread in the calculated values. As discussed above, this is likely due to the low values of the $<D_{\alpha\alpha}>$ from the BAS model in this MLT sector which are causing an exponential drop off in flux in the loss cone (see Figure 3b). Each plot gives the Pearson linear correlation coefficient (r) for the measured and calculated T0 precipitation and also notes the number of data points (N) in each L^*/MLT sector that meet our criteria for analysis. The correlation is higher in the 09–12 MLT sector compared to the 21–24 MLT sector

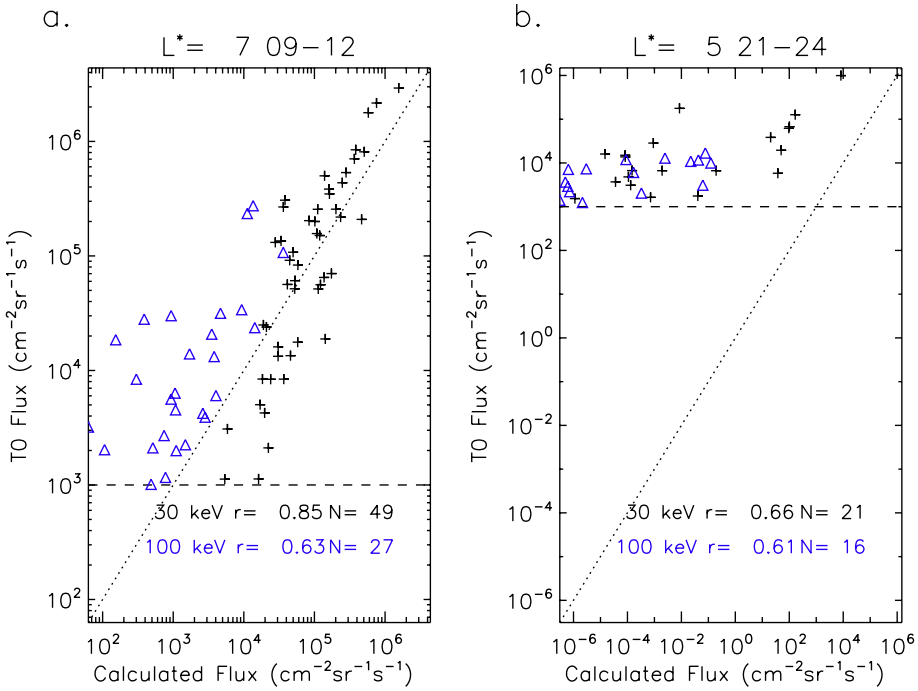

Figure 7. Figures demonstrating the correlation between the measured and calculated T0 precipitation for (a) $L^* = 6$, 09–12 MLT and (b) $L^* = 5$, 21–24 MLT as black crosses and blue triangles for the >30 keV and >100 keV channels respectively. The horizontal dashed line shows the noise threshold from our criteria.

for each energy channel and in both MLT sectors the correlation is higher for the >30 keV channel than the >100 keV channel.

Figure 8 shows the global linear correlation (given by the color) between the calculated T0 precipitation and that measured by the POES T0 > 30 keV channel during the event at 3 h MLT and 0.5 L^* resolution between $L^* = 4$ and 8. This is calculated as demonstrated in Figures 6 and 7 but is only shown where the confidence level is above 95% (less than 0.05 significance). Overall, the results show higher correlation between the measured and calculated precipitation on the dawnside than the duskside, although we note that there are less statistically significant results on the duskside (this is due to smaller correlations needing more data points to be statistically significant). We do not show the results from the >100 kev channel as there are not enough data to make the results statistically significant, however we see a similar pattern with higher correlations on the dawnside at $L^* > 5$. Figure 8, demonstrates that we find the best agreement for the >30 keV electrons between 06–12 MLT for $L^* > 5$ and between 03–06 MLT for L^* from 4.5 to 6; this pattern is very similar to that seen for the chorus $<D_{\alpha\alpha}>$ at 30 keV shown in Figure 1.

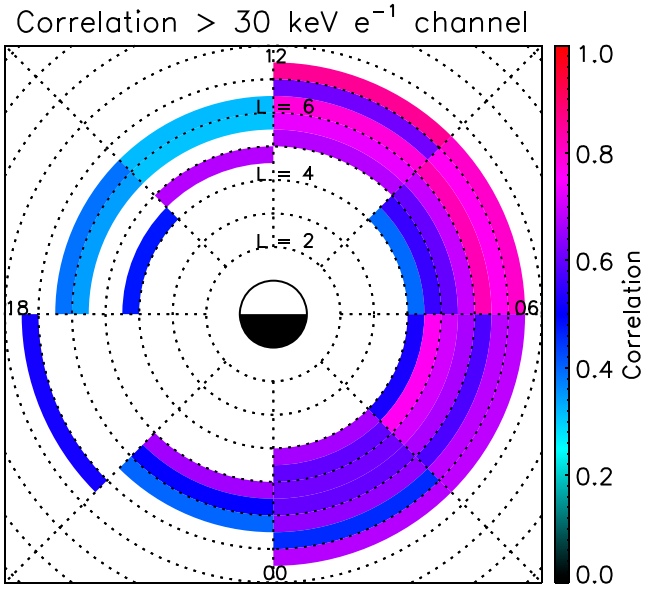

Figure 8. Figure showing the linear correlation between the precipitation calculated from the BAS-RBM diffusion coefficients and the precipitation measured by POES. The correlation is only shown where the confidence level is above 95%.

Figure 9 shows the ratio of the calculated and measured T0 precipitation flux for a range of MLT sectors and L-shells as a function of Kp* (larger of the current Kp or the Kp averaged over the last 12 h). The best agreement between the measured and calculated T0 flux occurs between 06–12 MLT at $L^* = 5$ and 6 for the >30 keV channel. There is a tendency for better agreement for higher Kp (particularly at $L^* = 5$, 06–12 MLT, for both > 30 keV and >100 keV), but it is not very strong. The measured flux is consistently higher than the calculated flux on the duskside (12–18 and 18–24 MLT sectors) and at all MLT's at $L^* = 4$. The calculations also underestimate the precipitation at most MLT's for the >100 keV channel.

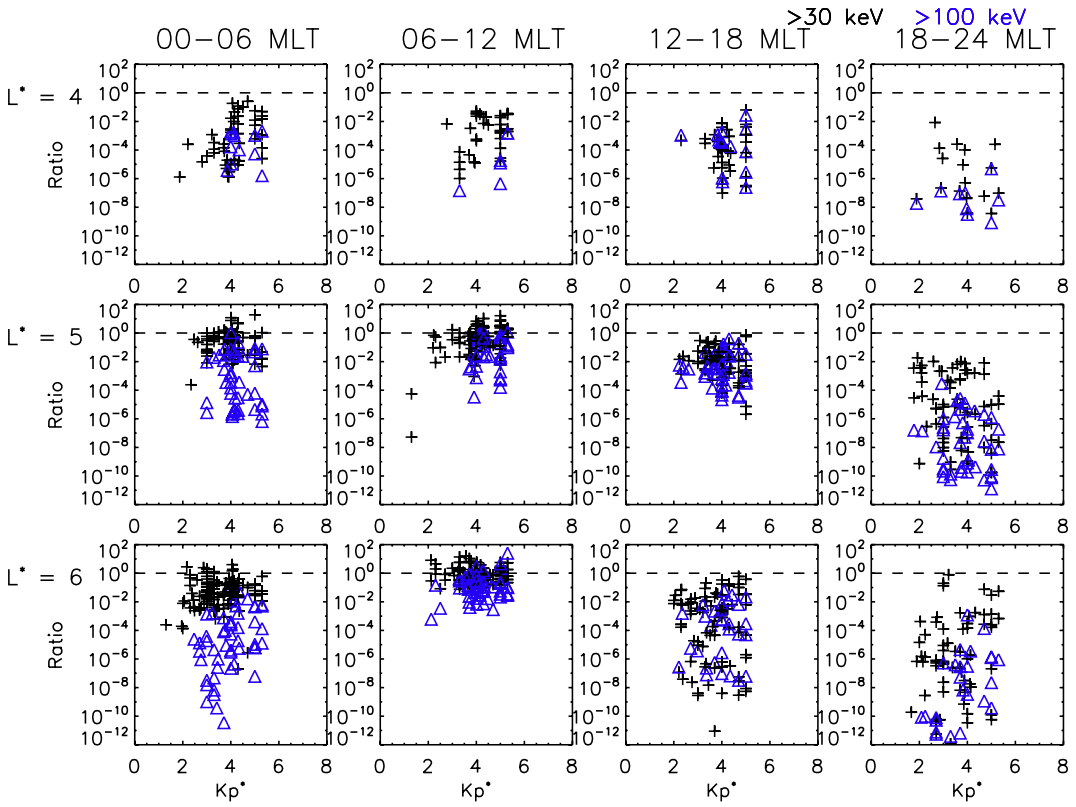

Figure 9. Plot showing the ratio between the calculated and measured T0 precipitation as a function of Kp* for a range of L^* and MLT sectors in black and blue for >30 keV and >100 keV channels. A dashed line is shown at $y = 1$ indicate perfect agreement between the model and the measurements and where the model is under (below the line) and over estimating the precipitation measured by POES (above the line).

These underestimates are fairly consistent over all geomagnetic activity levels and the possible reasons are discussed in Section 5.

4.2. Loss Cone Reconstruction

As demonstrated by Figure 3, the steady state solutions from Kennel and Petschek (1966) (Equations 3 and 4) can be used to simulate the flux over the entire loss cone for different levels of pitch angle diffusion. In the above analysis we calculated the theoretical flux that would be measured inside the field of view of the POES T0 detector but as we can see from Figure 3, the T0 FOV does not cover the entire loss cone. Below we repeat our calculation shown in Equation 8 but now integrate over the entire loss cone,

$$J_{LC}(E > E_{th}) = \frac{2\pi \int_{E_{th}}^{E_{max}} \int_0^{\alpha_0} J_{eq}(E, \alpha_{eq}) \sin\alpha \, d\alpha dE}{2\pi \int_0^{\alpha_0} \sin\alpha \, d\alpha}, \quad (10)$$

where $J_{eq}(E, \alpha_{eq})$ is the flux calculated from Equation 4.

Figure 10 shows the ratio of the calculated flux measured by POES T0 (J_{calc}, from Equations 3 to 8) and the total flux in the loss cone (J_{LC}) for the >30 keV electron channel as a function of Kp* at $L^* = 6$, 6.5, and 7 for 06–09 MLT (where we get good agreement between our analysis and the POES measurements, as demonstrated by Figure 8). Figure 10 shows the ratio predominately varies between 1 and 10, with some higher ratio values during low Kp*; the second panel of Figure 10, for $L^* = 6.5$, there is one instance where the ratio is almost 60 at Kp* = 1. This suggests that the calculated T0 flux misses a higher percentage of the precipitating flux during lower geomagnetic activity. Lines of best fit are included on each panel showing that the

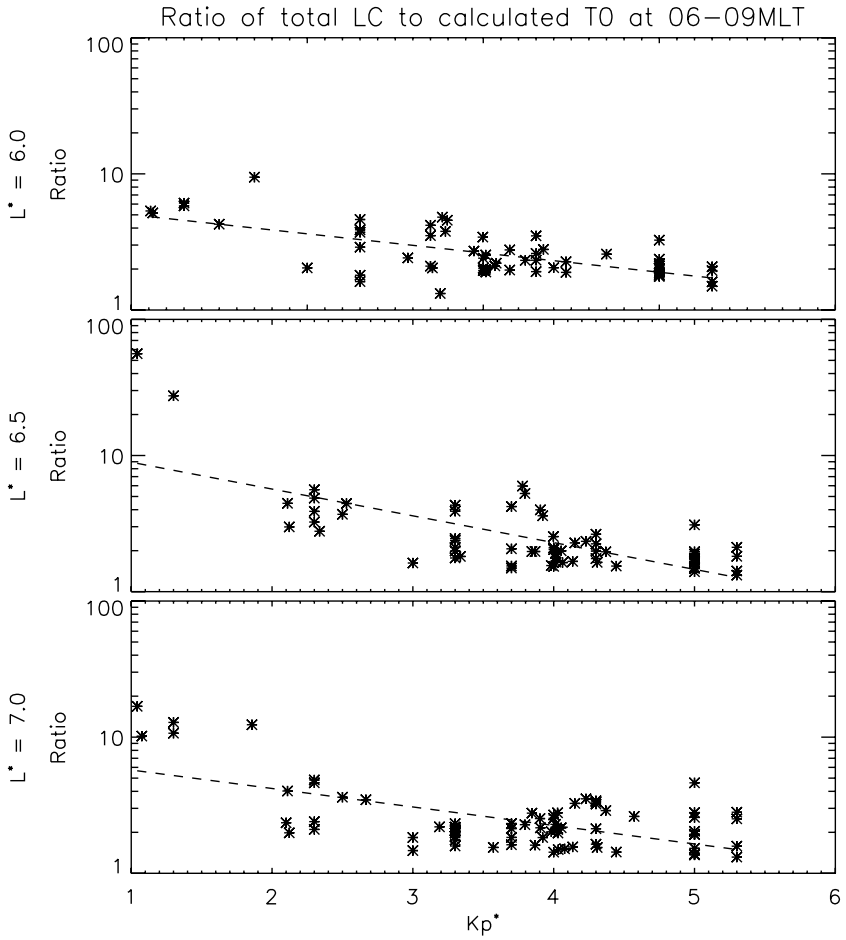

Figure 10. Figure showing the ratio of the calculated precipitation over the entire loss cone and the calculated precipitation inside the T0 FOV at $L^* = 6, 6.5, 7$ between 06–09 MLT as a function of Kp*. Lines of best fit are indicated in each panel by dashed lines.

ratio is decreasing with increasing Kp*. This relation is in agreement with previous studies who have tried to correct for the T0 FOV, for example, Rodger et al. (2013).

5. Discussion

Bounce-averaged pitch angle diffusion coefficients from the BAS-RBM have been used to calculate electron precipitation and compared to POES data. The results show better agreement between the calculated and measured T0 flux for $L^* > 5$ between 06–12 MLT and $L^* = 4.5$–6 between 03–06 MLT for >30 keV electron precipitation (see Figure 8). Indeed, the global distribution of the best correlation (Figure 8) closely resembles the global chorus $<D_{\alpha\alpha}>$ at 30 keV shown in Figure 1, suggesting that chorus wave are responsible for the bulk of the precipitation in these regions. We find better agreement between the calculated precipitating flux at >30 keV than at >100 keV for all levels of activity which suggests we may be missing a process which more efficiently scatters higher energy electrons.

We demonstrated a novel method to reconstruct the precipitation over the entire loss cone from the BAS-RBM diffusion coefficients, as demonstrated in Section 4.2. We found that the difference between the total calculated flux in the loss cone and the calculated flux in the T0 FOV varied predominately between 1 and 10 (see Figure 10); there are cases where the ratio is higher during low Kp. However, we note that the largest disagreements between our calculated and the measured T0 flux are when geomagnetic conditions are at their quietest and therefore these high ratios may be a product of our method underestimating the T0 flux. Our results are in agreement with those found by Nesse Tyssøy et al. (2016); in their study they

evaluate similar wave-particle interaction formulations to those presented in this paper to construct the entire bounce loss cone, finding the ratio to be around 1 during active conditions and up to 10 during moderate geomagnetic conditions. Our results are also consistent with Rodger et al. (2013) who found, by comparison with riometer data in northern Finland, that during periods of high precipitation the riometer and POES observations agreed well but during quieter times, the POES instruments were underestimating the flux by 7–9 times. The fact our results are consistent with previous work is promising for adopting this analysis, after further checks, to account for the electron precipitation input currently missed by the POES T0 detector (which has been used to quantify the precipitation in the CMIP6 data set).

There are times where the method presented in this paper underestimates the calculated T0 precipitating flux (e.g., at higher energies and on the duskside, see Figure 9), suggesting that some additional diffusion is required in the BAS wave model. This low loss rate could mean that the trapped flux in simulations run with the BAS-RBM may be over-estimated. However, if the lack of precipitation is due, for example, to insufficient chorus wave power then this means that acceleration due to chorus is also underestimated, and hence the trapped flux would be underestimated. At this stage it is not easy to say what the net effect on the BAS-RBM model output would be as it would depend on the time history of the event.

There are several reasons we might expect to see differences between the measured and calculated T0 fluxes, including the fact we are using averaged wave models (described in Section 2.1) which are unlikely to capture all of the variations of the wave power during this specific period. As pointed out by one referee, Figure 2 of Ripoll et al. (2017) show the RBSP hiss activity during the event studied in this paper (26–30 March 2013), in which the plasma density has successive narrow falls off, making this period quite complex. Using event specific conditions, Ripoll et al. (2019) calculated drift averaged diffusion coefficients for hiss waves of the order of 3×10^{-4} s^{-1} for 100 keV electrons around $L = 4.5$–5.5 during quiet times in March 2013. This is significantly higher than those used in this study for 100 keV electrons at $L^* = 5$, shown in the bottom row of Figure 6b, which could suggest we are underestimating the precipitation in this region due to underestimating the effects of hiss waves. As described in Section 2.1, the BAS diffusion coefficients are calculated using a modeled plasmapause and averaged values of f_{pe}/f_{ce}. Figure 4 of Ripoll et al. (2017) shows observations of f_{pe}/f_{ce} during this event which indicate the plasmapause reaches up to $L = 5.5$ on March 26, 2016 (perhaps further as the plot is limited to $L = 5.5$). The yellow line in Figure 1 represents the modeled plasmapause used in the calculation of the BAS diffusion coefficients, it is dashed between 14 and 22 MLT to indicate more work is needed to determine the average location in this region as it is possible it could extend out to larger L, as suggested by the observations from Ripoll et al. (2017). These observations demonstrate how variable the conditions are and hence how difficult it is to match the POES observations when using diffusion coefficients calculated from averaged wave properties. However, event-driven pitch angle diffusion coefficients are yet to be validated against observed precipitation, as is presented in this paper.

Figure 3 demonstrates that when the diffusion coefficients are small, the steady state solutions from Kennel and Petschek (1966) (Equations 3 and 4) will give an exponential drop off in flux close to the outer boundary of the bounce loss cone, likely outside the FOV of POES T0. Potential candidates for this missing contribution include hiss and chorus waves (as discussed above), EMIC waves (e.g., Clilverd et al., 2015; Denton et al., 2019; Hendry et al., 2017, 2019; Rodger et al., 2015) and magnetosonic waves (Horne et al., 2007). The best way to further explore this is by applying our method to more events, a statistical study would be a particularly good test of the average wave model and allow us to determine how much precipitation is driven by chorus waves.

The method we are applying to calculate the precipitation could also be a source of error in our analysis. We previously noted that by using the equations from Kennel and Petschek (1966), we are assuming steady state diffusion. This assumption has been adopted and validated by other studies (e.g., Li et al., 2013; Nesse Tyssøy et al., 2016) however, it could lead to an underestimate in the flux if there is bursty rather than continuous precipitation i.e. if we are not in a steady state. Furthermore, we take the T90 measurement as our source term which is converted to differential flux assuming a kappa distribution. We can see from Equations 3 and 4 that increasing the source term would directly increase the flux in the loss cone and therefore a problem with our source term may account for some of our underestimation. The T90 data itself could result in our method underestimating the precipitation as, although we exclude times when the field of view is inside the bounce loss cone and when the POES crosses the longitude associated with the South Atlantic

Anomaly, we have not accounted for times when it is measuring the drift loss cone (Rodger et al., 2010). This could mean T90 is underestimating the trapped flux which will result in our source term (and hence our precipitation) being underestimated. Lastly, the assumptions used in the kappa distribution could lead to some error in our calculated precipitation. Whittaker et al. (2013) found, by comparison to DEMETER data (a similar pitch angle resolution instrument to POES T90 but with better energy resolution), that a kappa distribution worked well to reproduce the spectra of radiation belt electron losses for $\kappa > 2$. In this study, we have assumed $\kappa = 5$ following Li et al. (2013), if we were to decrease the value of κ it would make our spectrum harder and perhaps improve our agreement for higher energies. All of these potential issues with our method could be investigated further with more studies.

6. Conclusions

We have tested the bounce averaged pitch angle diffusion coefficients from in the BAS radiation belt electron model by using them to calculate electron precipitation and comparing the results to measurements from POES. Our principle results are:

1. The agreement between the calculated flux and the POES data is much better on the dawn and dayside than in the afternoon sector for $L^* > 5$. This agreement is consistent with chorus being the dominant scattering mechanism in this MLT and L-shell zone, and that chorus-driven scattering is well represented in the model
2. We find better agreement between the calculated precipitating flux at >30 keV than at >100 for all levels of activity. This suggests we may be missing a process, or underestimating hiss wave effects, which more efficiently scatters higher energy electrons; we may also be underestimating the source spectrum at higher energies
3. Our results show that, due to the limited field of view, the total precipitating flux can exceed that measured by POES by a factor that varies from 1 to 10, which is in agreement with previous work
4. While there is likely to be a large uncertainty between our calculated precipitation and that measured by POES due to, for example, averaging of the wave data which are used to calculate the diffusion rates and the sampling of the data during the event in question, the calculated flux is consistently lower in some regions. This suggests that some additional diffusion is required to explain the flux at higher energies, and the flux on the dusk side. The effect of this underestimated loss suggests that the trapped flux simulated by the BAS-RBM might be over-estimated. However, more investigations are required before the net effect on the BAS-RBM output can be quantified. As noted in the Discussion the differences could also be due to the method, that is, either the assumption of steady state or the value of kappa

Data Availability Statement

The POES particle data used in this study came from NOAA National Geophysical Data Centre for the (https://ngdc.noaa.gov/stp/satellite/poes/dataaccess.html). The authors thank Janet Green for her bow tie analysis software. The Kp an Dst indices were downloaded from the OMNI database (https://omniweb.gsfc.nasa.gov/). The data used in this paper are available from the U.K. Polar Data Centre (https://doi.org/10.5285/1ccb7d38-48d8-4206-be34-b218fa763b5a). The authors would like to thank the referees for their helpful comments and improvements to the paper.

Acknowledgments
This work was supported by NERC Highlight Topic Grant NE/P01738X/1 (Rad-Sat) and NERC National Capability grants NE/R016038/1 and NE/R016445/1.

References

Abel, B., & Thorne, R. M. (1998). Electron scattering loss in Earth's inner magnetosphere: 1. Dominant physical processes. *Journal of Geophysical Research*, *103*(A2), 2385–2396. https://doi.org/10.1029/97JA02919

Albert, J. M., Meredith, N. P., & Horne, R. B. (2009). Three-dimensional diffusion simulation of outer radiation belt electrons during the 9 October 1990 magnetic storm. *Journal of Geophysical Research*, *114*(A9), A09214. https://doi.org/10.1029/2009JA014336

Allison, H. J., Horne, R. B., Glauert, S. A., & Del Zanna, G. (2018). Determination of the equatorial electron differential flux from observations at low Earth orbit. *Journal of Geophysical Research: Space Physics*, *123*(11), 9574–9596. https://doi.org/10.1029/2018JA025786

Andersson, M. E., Verronen, P. T., Marsh, D. R., Seppälä, A., Päivärinta, S. M., Rodger, C. J., et al. (2018). Polar ozone response to energetic particle precipitation over decadal time scales: The role of medium-energy electrons. *Journal of Geophysical Research*, *123*(1), 607–622. https://doi.org/10.1002/2017JD027605

Andersson, M. E., Verronen, P. T., Rodger, C. J., Clilverd, M. A., & Seppälä, A. (2014). Missing driver in the Sun-Earth connection from energetic electron precipitation impacts mesospheric ozone. *Nature Communications*, *5*, 5197. https://doi.org/10.1038/ncomms6197

Baker, D., Belian, R., Higbie, P., Klebesadel, R., & Blake, J. (1987). Deep dielectric charging effects due to high-energy electrons in Earth's outer magnetosphere. *Journal of Electrostatics*, *20*(1), 3–19. https://doi.org/10.1016/0304-3886(87)90082-9

Baumgaertner, A. J. G., Seppälä, A., Jöckel, P., & Clilverd, M. A. (2011). Geomagnetic activity related NO_x enhancements and polar surface air temperature variability in a chemistry climate model: Modulation of the NAM index. *Atmospheric Chemistry and Physics*, *11*(9), 4521–4531. https://doi.org/10.5194/acp-11-4521-2011

Carpenter, D. L., & Anderson, R. R. (1992). An ISEE/whistler model of equatorial electron density in the magnetosphere. *Journal of Geophysical Research*, *97*(A2), 1097–1108. https://doi.org/10.1029/91JA01548

Clilverd, M. A., Duthie, R., Hardman, R., Hendry, A. T., Rodger, C. J., Raita, T., et al. (2015). Electron precipitation from EMIC waves: A case study from 31 May 2013. *Journal of Geophysical Research: Space Physics*, *120*(5), 3618–3631. https://doi.org/10.1002/2015JA021090

Cunningham, G. S., Loridan, V., Ripoll, J.-F., & Schulz, M. (2018). Neoclassical diffusion of radiation-belt electrons across very low L-shells. *Journal of Geophysical Research: Space Physics*, *123*(4), 2884–2901. https://doi.org/10.1002/2017JA024931

Denton, R. E., Ofman, L., Shprits, Y. Y., Bortnik, J., Millan, R. M., Rodger, C. J., et al. (2019). Pitch angle scattering of sub-MeV relativistic electrons by electromagnetic ion cyclotron waves. *Journal of Geophysical Research: Space Physics*, *124*(7), 5610–5626. https://doi.org/10.1029/2018JA026384

Evans, D., & Greer, M. (2004). Polar orbiting environmental satellite space environment monitor - 2 instrument descriptions and archive data documentation. *NOAA Technical Memorandum 1.4*. Boulder, CO: Space Environment Laboratory.

Ferradas, C. P., Jordanova, V. K., Reeves, G. D., & Larsen, B. A. (2019). Comparison of electron loss models in the inner magnetosphere during the 2013 St. Patrick's Day geomagnetic storm. *Journal of Geophysical Research: Space Physics*, *124*(10), 7872–7888. https://doi.org/10.1029/2019JA026649

Gallagher, D. L., Craven, P. D., & Comfort, R. H. (2000). Global core plasma model. *Journal of Geophysical Research*, *105*(A8), 18819–18833. https://doi.org/10.1029/1999JA000241

Glauert, S. A., & Horne, R. B. (2005). Calculation of pitch angle and energy diffusion coefficients with the PADIE code. *Journal of Geophysical Research*, *110*(A4), A04206. https://doi.org/10.1029/2004JA010851

Glauert, S. A., Horne, R. B., & Meredith, N. P. (2014). Three-dimensional electron radiation belt simulations using the BAS Radiation Belt Model with new diffusion models for chorus, plasmaspheric hiss, and lightning-generated whistlers. *Journal of Geophysical Research: Space Physics*, *119*(1), 268–289. https://doi.org/10.1002/2013JA019281

Glauert, S. A., Horne, R. B., & Meredith, N. P. (2018). A 30-year simulation of the outer electron radiation belt. *Space Weather*, *16*(10), 1498–1522. https://doi.org/10.1029/2018SW001981

Hendry, A. T., Rodger, C. J., & Clilverd, M. A. (2017). Evidence of sub-MeV EMIC-driven electron precipitation. *Geophysical Research Letters*, *44*(3), 1210–1218. https://doi.org/10.1002/2016GL071807

Hendry, A. T., Santolik, O., Kletzing, C. A., Rodger, C. J., Shiokawa, K., & Baishev, D. (2019). Multi-instrument observation of nonlinear EMIC-driven electron precipitation at sub-MeV energies. *Geophysical Research Letters*, *46*(13), 7248–7257. https://doi.org/10.1029/2019GL082401

Horne, R. B., Kersten, T., Glauert, S. A., Meredith, N. P., Boscher, D., Sicard-Piet, A., et al. (2013). A new diffusion matrix for whistler mode chorus waves. *Journal of Geophysical Research: Space Physics*, *118*(10), 6302–6318. https://doi.org/10.1002/jgra.50594

Horne, R. B., Lam, M. M., & Green, J. C. (2009). Energetic electron precipitation from the outer radiation belt during geomagnetic storms. *Geophysics Research Letters*, *36*(19), L19104. https://doi.org/10.1029/2009GL040236

Horne, R. B., Thorne, R. M., Glauert, S. A., Albert, J. M., Meredith, N. P., & Anderson, R. R. (2005). Timescale for radiation belt electron acceleration by whistler mode chorus waves. *Journal of Geophysical Research*, *110*(A3), A03225. https://doi.org/10.1029/2004JA010811

Horne, R. B., Thorne, R. M., Glauert, S. A., Meredith, N. P., Pokhotelov, D., & Santolík, O. (2007). Electron acceleration in the Van Allen radiation belts by fast magnetosonic waves. *Geophysical Research Letters*, *34*(17), L17107. https://doi.org/10.1029/2007GL030267

Jordanova, V. K., Tu, W., Chen, Y., Morley, S. K., Panaitescu, A. D., Reeves, G. D., & Kletzing, C. A. (2016). RAM-SCB simulations of electron transport and plasma wave scattering during the October 2012 “double-dip” storm. *Journal of Geophysical Research: Space Physics*, *121*(9), 8712–8727. https://doi.org/10.1002/2016JA022470

Kennel, C. F., & Petschek, H. E. (1966). Limit on stably trapped particle fluxes. *Journal of Geophysical Research*, *71*(1), 1–28. https://doi.org/10.1029/JZ071i001p00001

Lam, M. M., Horne, R. B., Meredith, N. P., Glauert, S. A., Moffat-Griffin, T., & Green, J. C. (2010). Origin of energetic electron precipitation >30 keV into the atmosphere. *Journal of Geophysical Research: Space Physics*, *115*(8), A00F08. https://doi.org/10.1029/2009JA014619

Li, W., Ni, B., Thorne, R. M., Bortnik, J., Green, J. C., Kletzing, C. A., & Hospodarsky, G. B. (2013). Constructing the global distribution of chorus wave intensity using measurements of electrons by the poes satellites and waves by the Van Allen Probes. *Geophysical Research Letters*, *40*(17), 4526–4532. https://doi.org/10.1002/grl.50920

Li, Z., Hudson, M., Jaynes, A., Boyd, A., Malaspina, D., Thaller, S., et al. (2014). Modeling gradual diffusion changes in radiation belt electron phase space density for the March 2013 Van Allen Probes case study. *Journal of Geophysical Research: Space Physics*, *119*(10), 8396–8403. https://doi.org/10.1002/2014JA020359

Matthes, K., Funke, B., Andersson, M. E., Barnard, L., Beer, J., Charbonneau, P., et al. (2017). Solar forcing for CMIP6 (v3.2). *Geoscientific Model Development*, *10*(6), 2247–2302. https://doi.org/10.5194/gmd-10-2247-2017

Meredith, N. P., Horne, R. B., & Anderson, R. R. (2008). Survey of magnetosonic waves and proton ring distributions in the Earth's inner magnetosphere. *Journal of Geophysical Research*, *113*(A6), A06213. https://doi.org/10.1029/2007JA012975

Meredith, N. P., Horne, R. B., Glauert, S. A., Baker, D. N., Kanekal, S. G., & Albert, J. M. (2009). Relativistic electron loss timescales in the slot region. *Journal of Geophysical Research*, *114*(A3), A03222. https://doi.org/10.1029/2008JA013889

Meredith, N. P., Horne, R. B., Kersten, T., Li, W., Bortnik, J., Sicard, A., & Yearby, K. H. (2018). Global model of plasmaspheric hiss From multiple satellite observations. *Journal of Geophysical Research: Space Physics*, *123*(6), 4526–4541. https://doi.org/10.1029/2018JA025226

Meredith, N. P., Horne, R. B., Lam, M. M., Denton, M. H., Borovsky, J. E., & Green, J. C. (2011). Energetic electron precipitation during high-speed solar wind stream driven storms. *Journal of Geophysical Research*, *116*(A5), A05223. https://doi.org/10.1029/2010JA016293

Meredith, N. P., Horne, R. B., Shen, X.-C., Li, W., & Bortnik, J. (2020). Global Model of Whistler Mode Chorus in the Near-Equatorial Region ($|\lambda_m| < 18°$). *Geophysical Research Letters*. *47*(11), e2020GL087311. https://doi.org/10.1002/2020GL087311

Meredith, N. P., Horne, R. B., Thorne, R. M., & Anderson, R. R. (2003). Favored regions for chorus-driven electron acceleration to relativistic energies in the Earth's outer radiation belt. *Geophysical Research Letters*, *30*(16). https://doi.org/10.1029/2003GL017698

Meredith, N. P., Horne, R. B., Thorne, R. M., Summers, D., & Anderson, R. R. (2004). Substorm dependence of plasmaspheric hiss. *Journal of Geophysical Research*, *109*(A6), A06209. https://doi.org/10.1029/2004JA010387

Nesse Tyssøy, H., Sandanger, M. I., Ødegaard, L.-K. G., Stadsnes, J., Aasnes, A., & Zawedde, A. E. (2016). Energetic electron precipitation into the middle atmosphere—Constructing the loss cone fluxes from MEPED POES. *Journal of Geophysical Research: Space Physics*, *121*(6), 5693–5707. https://doi.org/10.1002/2016JA022752

Olson, W. P., & Pfitzer, K. A. (1977). *Magnetospheric magnetic field modeling. Annual scientific report*. Air Force Office of Scientific Research.

Orsolini, Y. J., Smith-Johnsen, C., Marsh, D. R., Stordal, F., Rodger, C. J., Verronen, P. T., & Clilverd, M. A. (2018). Mesospheric nitric acid enhancements during energetic electron precipitation events simulated by WACCM-D. *Journal of Geophysical Research: Atmospheres*, *123*(13), 6984–6998. https://doi.org/10.1029/2017JD028211

Picone, J. M., Hedin, A. E., Drob, D. P., & Aikin, A. C. (2002). NRLMSISE-00 empirical model of the atmosphere: Statistical comparisons and scientific issues. *Journal of Geophysical Research*, *107*(A12). SIA 15-1–SIA 15-16. https://doi.org/10.1029/2002JA009430

Ripoll, J. F., Loridan, V., Denton, M. H., Cunningham, G., Reeves, G., Santolík, O., et al. (2019). Observations and Fokker-Planck Simulations of the *L*-Shell, Energy, and Pitch Angle Structure of Earth's Electron Radiation Belts During Quiet Times. *Journal of Geophysical Research: Space Physics*, *124*(2), 1125–1142. https://doi.org/10.1029/2018JA026111

Ripoll, J. F., Santolík, O., Reeves, G. D., Kurth, W. S., Denton, M. H., Loridan, V., et al. (2017). Effects of whistler mode hiss waves in March 2013. *Journal of Geophysical Research: Space Physics*, *122*(7), 7433–7462. https://doi.org/10.1002/2017JA024139

Rodger, C. J., Carson, B. R., Cummer, S. A., Gamble, R. J., Clilverd, M. A., Green, J. C., et al. (2010a). Contrasting the efficiency of radiation belt losses caused by ducted and nonducted whistler-mode waves from ground-based transmitters. *Journal of Geophysical Research*, *115*(A12). https://doi.org/10.1029/2010JA015880

Rodger, C. J., Clilverd, M. A., Green, J. C., & Lam, M. M. (2010b). Use of POES SEM-2 observations to examine radiation belt dynamics and energetic electron precipitation into the atmosphere. *Journal of Geophysical Research*, *115*(A4). https://doi.org/10.1029/2008JA014023

Rodger, C. J., Hendry, A. T., Clilverd, M. A., Kletzing, C. A., Brundell, J. B., & Reeves, G. D. (2015). High-resolution in situ observations of electron precipitation-causing EMIC waves. *Geophysical Research Letters*, *42*(22), 9633–9641. https://doi.org/10.1002/2015GL066581

Rodger, C. J., Kavanagh, A. J., Clilverd, M. A., & Marple, S. R. (2013). Comparison between POES energetic electron precipitation observations and riometer absorptions: Implications for determining true precipitation fluxes. *Journal of Geophysical Research: Space Physics*, *118*(12), 7810–7821. https://doi.org/10.1002/2013JA019439

Rozanov, E., Callis, L., Schlesinger, M., Yang, F., Andronova, N., & Zubov, V. (2005). Atmospheric response to NO_y source due to energetic electron precipitation. *Geophysical Research Letters*, *32*(14). https://doi.org/10.1029/2005GL023041

Selesnick, R. S. (2012). Atmospheric scattering and decay of inner radiation belt electrons. *Journal of Geophysical Research: Space Physics*, *117*(A8), A08218. https://doi.org/10.1029/2012JA017793

Seppälä, A., Randall, C. E., Clilverd, M. A., Rozanov, E., & Rodger, C. J. (2009). Geomagnetic activity and polar surface air temperature variability. *Journal of Geophysical Research: Space Physics*, *114*(A10). https://doi.org/10.1029/2008JA014029

Shprits, Y. Y., Kellerman, A. C., Drozdov, A. Y., Spence, H. E., Reeves, G. D., & Baker, D. N. (2015). Combined convective and diffusive simulations: VERB-4D comparison with 17 March 2013 Van Allen Probes observations. *Geophysical Research Letters*, *42*(22), 9600–9608. https://doi.org/10.1002/2015GL065230

Subbotin, D., Shprits, Y., & Ni, B. (2010). Three-dimensional VERB radiation belt simulations including mixed diffusion. *Journal of Geophysical Research*, *115*(A3), A03205. https://doi.org/10.1029/2009JA015070

Summers, D., & Thorne, R. M. (2003). Relativistic electron pitch-angle scattering by electromagnetic ion cyclotron waves during geomagnetic storms. *Journal of Geophysical Research*, *108*(A4), 1143. https://doi.org/10.1029/2002JA009489

Theodoridis, G. C., & Paolini, F. R. (1967). Pitch angle diffusion of relativistic outer belt electrons. *Annales de Geophysique*, *23*(3), 375.

Thorne, R. (1977). Energetic radiation belt electron precipitation: A natural depletion mechanism for stratospheric ozone. *Science*, *195*(4275), 287–289. https://doi.org/10.1126/science.195.4275.287

Tsyganenko, N. A. (1995). Modeling the Earth's magnetospheric magnetic field confined within a realistic magnetopause. *Journal of Geophysical Research: Space Physics*, *100*(A4), 5599–5612. https://doi.org/10.1029/94JA03193

Van de Kamp, M., Rodger, C. J., Seppälä, A., Clilverd, M. A., & Verronen, P. T. (2018). An updated model providing long-term data sets of energetic electron precipitation, including zonal dependence. *Journal of Geophysical Research: Atmospheres*, *123*(17), 9891–9915. https://doi.org/10.1029/2017JD028253

Van de Kamp, M., Seppälä, A., Clilverd, M. A., Rodger, C. J., Verronen, P. T., & Whittaker, I. C. (2016). A model providing long-term data sets of energetic electron precipitation during geomagnetic storms. *Journal of Geophysical Research: Atmospheres*, *121*(20). 12520–12540. https://doi.org/10.1002/2015JD024212

Walt, M. (1994). *Introduction to geomagnetically trapped radiation*. Cambridge University Press. https://doi.org/10.1017/CBO9780511524981

Whittaker, I. C., Gamble, R. J., Rodger, C. J., Clilverd, M. A., & Sauvaud, J.-A. (2013). Determining the spectra of radiation belt electron losses: Fitting demeter electron flux observations for typical and storm times. *Journal of Geophysical Research: Space Physics*, *118*(12), 7611–7623. https://doi.org/10.1002/2013JA019228

Xiao, F., Shen, C., Wang, Y., Zheng, H., & Wang, S. (2008). Energetic electron distributions fitted with a relativistic kappa-type function at geosynchronous orbit. *Journal of Geophysical Research: Space Physics*, *113*(A5). https://doi.org/10.1029/2007JA012903

Xiao, F., Yang, C., He, Z., Su, Z., Zhou, Q., He, Y., et al. (2014). Chorus acceleration of radiation belt relativistic electrons during March 2013 geomagnetic storm. *Journal of Geophysical Research: Space Physics*, *119*(5), 3325–3332. https://doi.org/10.1002/2014JA019822

Yando, K., Millan, R. M., Green, J. C., & Evans, D. S. (2011). A Monte Carlo simulation of the NOAA POES medium energy proton and electron detector instrument. *Journal of Geophysical Research: Space Physics*, *116*(A10), A10231. https://doi.org/10.1029/2011JA016671